ARTICLE   OPEN

Multi-experiment nonlinear mixed effect modeling of single-cell translation kinetics after transfection

Fabian Fröhlich [1,2], Anita Reiser[3], Laura Fink[3], Daniel Woschée[3], Thomas Ligon[3], Fabian Joachim Theis [1,2], Joachim Oskar Rädler[3] and Jan Hasenauer [1,2,4]

Single-cell time-lapse studies have advanced the quantitative understanding of cellular pathways and their inherent cell-to-cell variability. However, parameters retrieved from individual experiments are model dependent and their estimation is limited, if based on solely one kind of experiment. Hence, methods to integrate data collected under different conditions are expected to improve model validation and information content. Here we present a multi-experiment nonlinear mixed effect modeling approach for mechanistic pathway models, which allows the integration of multiple single-cell perturbation experiments. We apply this approach to the translation of green fluorescent protein after transfection using a massively parallel read-out of micropatterned single-cell arrays. We demonstrate that the integration of data from perturbation experiments allows the robust reconstruction of cell-to-cell variability, i.e., parameter densities, while each individual experiment provides insufficient information. Indeed, we show that the integration of the datasets on the population level also improves the estimates for individual cells by breaking symmetries, although each of them is only measured in one experiment. Moreover, we confirmed that the suggested approach is robust with respect to batch effects across experimental replicates and can provide mechanistic insights into the nature of batch effects. We anticipate that the proposed multi-experiment nonlinear mixed effect modeling approach will serve as a basis for the analysis of cellular heterogeneity in single-cell dynamics.

npj Systems Biology and Applications (2019)5:1 ; https://doi.org/10.1038/s41540-018-0079-7

INTRODUCTION

Living cells show molecular and phenotypic differences at the single-cell level even in isogenic populations.[1,2] Sources of cell-to-cell variability include noisy cellular processes,[2] differences in cell cycle state,[3] the history of individual cells,[4] as well as spatio-temporal differences of the cell's environment.[5] Methods such as mass cytometry[6] or single-cell RNA sequencing[7] can provide highly multiplexed snapshots of cell-to-cell variability in thousands to millions of cells. Complementarily, time-lapse microscopy allows for the time-resolved measurement of cell-to-cell variability in the dynamic response of cells.[8,9] Recently, in order to improve the high-throughput capability of single-cell time-lapse studies, microstructured arrays[8,10] or microfluidic devices[11] are used to restrict cells in their movement, enabling automated acquisition of single-cell fluorescence trajectories over time.

Single-cell technologies already facilitated many novel insights, ranging from the analysis of population structures[3,6] over the assessment of developmental trajectories[12,13] to mechanistic insights into causal differences.[2,14–16] To gain mechanistic insights, many studies use ordinary differential equation (ODE) models.[17–20]

In this spirit, earlier studies have analyzed time-lapse micro-scopy measurements of single-cells after transfection with synthetic mRNA to assess mRNA lifetime.[21] mRNA lifetime is of fundamental interest to basic science, as it is a key parameter in many gene regulatory processes. Moreover, transient transfection of synthetic mRNA is relevant for biomedical applications, as it enables treatment of diseases via the targeted expression of proteins.[22,23] Hence, a good understanding and control of the expression dynamics of therapeutic proteins is essential for treatment design.[24] Yet, inference of quantitative estimates from single-cell experiments is model dependent and only insofar meaningful as our mechanistic understanding of many basic cellular processes, including transcription and translation, is sufficiently accurate. The model parameters can be estimated from single-cell time-lapse microscopy measurements using two different approaches:

(I)   The standard two-stage approach (STS) estimates single-cell parameters and population distribution parameters sequentially.[25,26] First, parameters for every single cell are estimated independently by fitting an ODE to the respective trajectory. Then, a population-wide parameter distribution is reconstructed according to the single-cell parameter estimates. The STS approach enjoys great popularity,[21,25–27] because it is easy to implement, as many methods and tools developed for bulk data can be applied. However, the STS approach fails to distinguish between cell-to-cell variability and uncertainty of the estimated single-cell parameters, resulting in the overestimation of cell-to-cell variability.[28] This impairs applicability of the STS approach in settings with high experimental noise and sparse observations.[26]

(II) In contrast, the non-linear mixed effect (NLME) approach[29] estimates single-cell parameters and population distribution parameters simultaneously. The single-cell parameters are considered as latent variables, which are constrained by the population distribution. The implementation of the NLME approach is more involved[30–32] and its application computationally more intensive. Originally developed in pharmacology,[32] the NLME approach has recently risen in popularity for the analysis of single-cell data.[25,26,33,34] It has been reported that NLME is more robust than STS in settings with large parameter uncertainty, as it reduces uncertainty[26,28] and removes estimation bias.[25]

The NLME approach has several advantages over the STS approach when single-cell parameters have poor practical identifiability,[26,28] i.e., when the amount or noisiness of the data prohibits reliable parameter estimation. However, structural non-identifiability[35] of single-cell parameters is problematic for the STS, as well as for the NMLE approach. Structural non-identifiabilities, meaning that the reliable parameter estimation is impossible due to model structure (vector field and observable), of single-cell parameters may lead to structural non-identifiability of population distribution parameters[36] and thus prohibit the reliable estimation of cell-to-cell variability. For bulk data, such structural non-identifiabilities can be resolved by considering perturbation experiments.[37] For single-cell data, it is unclear how the consideration of perturbation experiments affects non-identifiability for the STS and NLME approach.

Previous studies have shown that the single-cell degradation rates of mRNAs and proteins are structurally non-identifiable when considering time-lapse microscopy measurements for a single protein.[10] This also holds for the respective population average parameters, as long as no further assumptions are made.[24] For this application, the structural non-identifiability is particularly problematic, as it impedes the reliable estimation of the mRNA lifetime, a key parameters of interest.

In this study, we address this problem by extending NLME to a multi-experiment setting, allowing the integration of single-cell perturbation experiments, which is not possible for the STS approach. We apply the method to study the fluorescence trajectories of individual cells after transfection with mRNA encoding for eGFP. The fluorescence trajectories are collected by combining time-lapse microscopy, micropatterned protein arrays and a perfusion tubing systems, enabling the assessment of hundreds of single cells in a controlled microenvironment. In contrast to previous studies, experiments were carried out twofold using two distinct variants of eGFP that differ in their protein lifetime. By analyzing single-cell trajectories from both experiments in a consistent nonlinear mixed effect modeling approach, we demonstrate that both protein and mRNA degradation rates can be uniquely identified. Furthermore, we assess the use of extended models for translation, including enzymatic degradation, as well as ribosomally limited translation and find evidence for ribosomal rate-limitation of the translation process. Moreover, we show that the developed approach enables the robust estimation of population parameters, despite the presence of batch effects.

RESULTS

Single-cell time-lapse experiments reveal a large heterogeneity of the fluorescent reporter protein expression after mRNA transfection

To obtain high-quality data of single-cell transfection-translation dynamics, we combined micropatterned protein arrays (Fig. 1a) with scanning time-lapse microscopy of multiple positions over a duration of 30 h (Fig. 1b) using a tailored perfusion tubing system. The perfusion tubing system allows for mRNA transfection during the time-lapse measurement. The micropatterned protein arrays simplify image processing and—even more important—ensure a standardized single-cell environment,[38] which improves the comparability between cells leading to better data quality.

The cells were incubated with mRNA lipoplexes (Lipofectamine2000^{TM}) during the first hour of the measurement and washed with cell culture medium afterwards to limit the time window for lipoplex uptake. After a cell successfully internalizes mRNA lipoplexes, the corresponding mRNA molecules are translated into fluorescent proteins. This translation processes can be described by biochemical rate equations (Fig. 1c).[21] The use of tubing systems allows for the observation of the translation kinetics of single cells right after adding mRNA lipoplexes (Fig. 1d), which was not possible in previous studies. The protein expression dynamics of single cells were measured by integration over the fluorescence intensities of successfully confined and transfected cells (at least 500 cells per mRNA construct and experiment). The analysis of the trajectories revealed substantial cell-to-cell variability in the amplitude and timing of expression. The collected data is available at https://doi.org/10.5281/zenodo.1228898.

Single-experiment single-cell measurements are insufficient for estimation of protein translation parameters

For an in-depth analysis of the collected single-cell trajectories, we employed mathematical modeling. The process model we used is based on the established two-stage model of gene expression[17] and describes the concentration of mRNA and GFP molecules over time:

$$\frac{d[\text{mRNA}]}{dt} = -\delta[\text{mRNA}], [\text{mRNA}](0) = 0, \quad \lim_{t \to t_0, t < t_0} [\text{mRNA}](t) = [\text{mRNA}](t) + m_0$$

$$\frac{d[\text{GFP}]}{dt} = k[\text{mRNA}] - \gamma[\text{GFP}], [\text{GFP}](0) = 0,$$

where k is the translation rate per mRNA, m_0 is the amount of transfected mRNA entering the cell at time point t_0, δ is the mRNA degradation rate and γ is the protein degradation rate. The output fluorescence y is assumed to be the sum of a signal proportional to the amount of eGFP (with scaling parameter $scale$) plus background fluorescence ($offset$). To facilitate the use of an additive error model, we consider the logarithm of the fluorescence intensity

$$y = \log(scale[\text{GFP}] + offset).$$

Not all of these parameters are structurally identifiable. Therefore, we transform the model and reduced the parameter vector to a set of parameters θ that consists of products of the original parameters. Model transformation was performed by normalizing the mRNA concentration with the amount of transfected mRNA m_0 and the GFP concentration with the scaling parameter $scale$. The transformed model only depends on the new combined parameter k, m_0, $scale$ instead of the three parameters k, m_0, $scale$. (see Methods, Section Mathematical Models For GFP Translation).

Following the literature,[25,26] we estimated all parameters using the STS approach (Fig. 2a). The parameters of individual cells were inferred from measured single-cell trajectories using a maximum likelihood method (stage 1) and then the distribution of parameters across the cell population was assessed (stage 2). The single-cell trajectories indicate pronounced cell-to-cell variability (Fig. 2b), which is reasonably well captured in the individual single-cell model fits (Fig. 2c). This pronounced cell-to-cell variability is in agreement with previous studies suggesting stochasticity of mRNA uptake[39] and limited enzyme abundances, as well as inhomogeneous spatial distribution within cells, e.g., for ribosomes.[40]
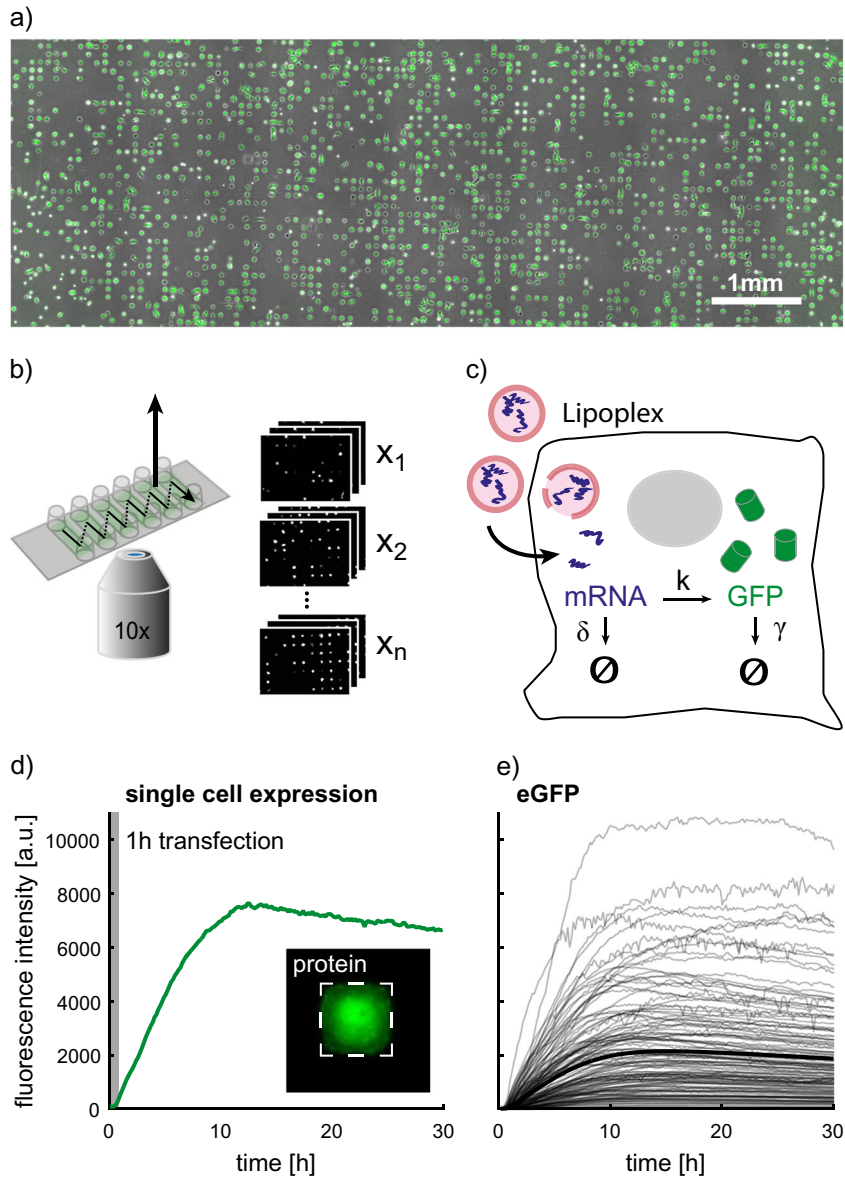
Fig. 1 Single-cell translation assay for highly parallel readout of reporter protein expression kinetics after mRNA transfection. **a** Micropatterned protein arrays are used for highly parallel readout of single-cell kinetics on standardized protein adhesion spots, which enables the observation of thousands of cells over a long time period. The microscopy image shows the micropatterned area of one channel with cells expressing eGFP. **b** Schematics of the six-channel sample holder and the scanning time-lapse acquisition mode. Stacks of images from individual panels are depicted on the right. **c** Schematic illustration of the transfection process using mRNA containing lipoplexes. The mRNA, which is released into the cytosol, is translated into a fluorescent reporter protein. The translation dynamics are modeled by biochemical rate equations. **d** Single-cell eGFP expression is measured by integration over the fluorescence intensity. The zoom-in shows one eGFP-expressing cell confined on a fibronectin square (dashed square). The recording of protein expression begins by adding the mRNA lipoplexes, which are incubated for 1 h. **e** A subset of the single-cell trajectories of eGFP expressing cells shows the heterogeneity within the population. The thick black trajectory corresponds to the mean protein expression dynamic

The parameter distributions of the degradation rates, δ and γ, span two orders of magnitude and indicate multiple modes (Fig. 2d). At first glance, this suggests a previously unidentified subpopulation structure. Yet, the careful examination of the model structure (see Methods, Section Uncertainty Analysis of Single-Cell Parameters) revealed symmetry in the two degradation rates, δ and γ. The numerical values of the parameters δ and γ can be interchanged without altering the time course of GFP. We found that this symmetry, instead of multiple subpopulations, gives rise to the particular shapes of the estimated parameter distributions. This symmetry in the parameter estimates corresponds to a global structural non-identifiability,[35] but indeed, the parameters are locally structurally identifiable.

Using structural identifiability analysis, we found that the symmetry could be resolved by (i) simultaneously measuring single-cell mRNA and protein levels or by (ii) measuring single-cell protein levels in cells sequentially transfected with different mRNA constructs. Both approaches are conceptually feasible (see for (i)[35,41,42]) but non-trivial. In general, the unique identification of relevant parameters from a single experiment is often challenging or impossible with the available experimental techniques. For bulk experiments, structural non-identifiabilities can sometimes be resolved by considering additional perturbation experiments.[43]
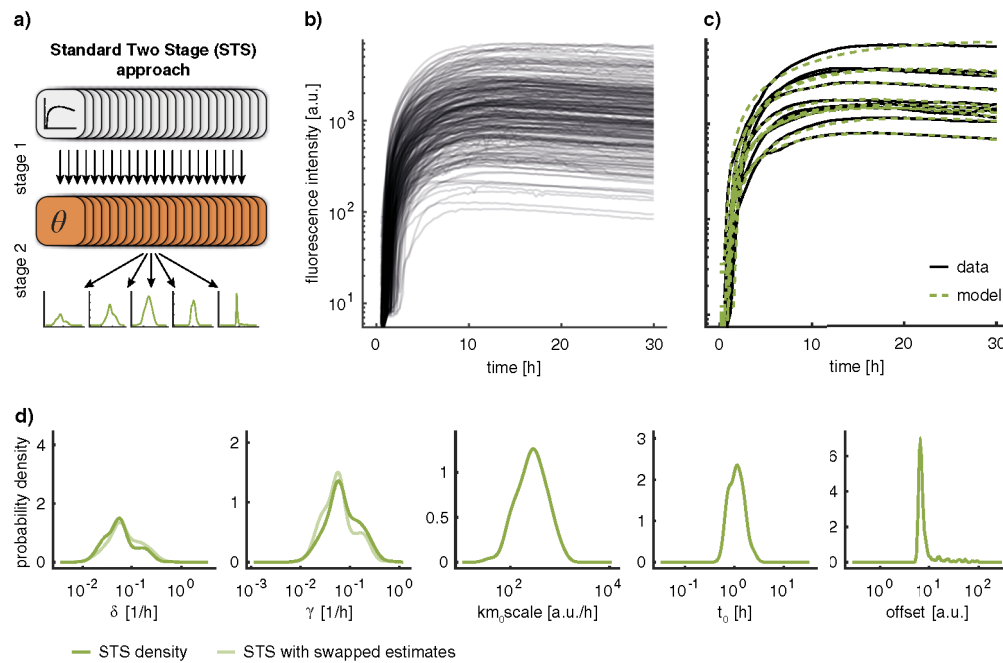
Fig. 2 Parameter estimation results for the STS approach. **a** Schematic illustration of the Standard Two-Stage (STS) approach. **b** Experimentally recorded single-cell eGFP trajectories. **c** Exemplary fits for 10 single-cell trajectories. **d** Parameter distributions computed according to the STS approach using a kernel density estimate. The symmetry in δ and γ is illustrated by showing the respective kernel density estimate if the estimated values are swapped in lighter color

This is possible as parameters can be assumed to be conserved quantities, which enables the recasting of perturbation experiments as additional observables in the model.[44] In contrast, it is non-trivial to consider additional perturbation experiments in the STS approach. For the STS approach, all single-cell parameters, and, hence, the parameter distributions for all experiments are assumed to be independent. Thus, no conserved quantities exist and information from multiple perturbation experiments cannot be exploited efficiently.

Multi-experiment NLME-modeling breaks parameter symmetry
To resolve the structural non-identifiability, we employed the NLME approach to integrate multiple perturbation experiments. In contrast to the STS approach, the NLME allows for conserved quantities between perturbation experiments (Fig. 3a). For the NLME model, we assume that the parameters φ_i of the ith single cell consist of a fixed effect β and a random effect $b_i \sim N(0, D)$: $\varphi_i = \exp(\beta + b_i)$. The population parameters β and D are the mean and the covariance of the logarithm of the single-cell parameters. This corresponds to a lognormal distribution assumption, which ensures positivity of single-cell parameters.

The population parameters β and D are conserved between experimental conditions, even if different individual cells are observed. Accordingly, single-cell data collected for different experiments can be integrated on the level of the cell population using β and D. In the NLME approach the population parameters β and D, as well as the single-cell parameters φ_i are estimated simultaneously in a hierarchical optimization problem (see Methods, Section NLME Approach).

To resolve the non-identifiability in the translation model, we recorded an additional dataset in which cells were transfected with destabilized eGFP (d2eGFP). The fluorescence intensity was quantified for single cells for a duration of 30 h after transfection. For cells transfected with eGFP the recorded signal reached a peak at around 9 h and remained stable for the rest of the experiment (Fig. 3b). For cells transfected with d2eGFP the signal peaked

around 10 h and declined subsequently. For both datasets a pronounced variability of the recorded trajectories is evident.

We used both datasets, eGFP and d2deGFP, to estimate parameters using the STS and the NLME approach. For the NLME we assume two distinct parameter distributions for the protein degradation rates (γ_{eGFP} for eGFP and γ_{d2eGFP} for d2eGFP) (see Methods, Section Multi-Experiment Extension of the NLME Approach). For all other parameters, including the mRNA degradation rate δ, the distributions are assumed to be identical across experiments. For the STS approach, we also assume that the protein degradation rates differ and calculate the corresponding parameter distributions for each experiment. However, it is not possible to enforce that the distributions of the remaining parameters are identical between the experiments.

The analysis of the optimization results revealed that the STS and the NLME approach yield almost identical fits to the single-cell data (Fig. 3c). Moreover, for the NLME approach, the distributions of the estimated single-cell parameters φ_i agreed with the estimated distribution parameters β and D (Fig. S3). In summary, this suggests that the distribution assumptions for the NLME were appropriate.

For most of the parameters (km_0scale, t_0, $offset$, and γ_{d2eGFP}), both approaches yield similar population distributions (Fig. 3d). This may be surprising for γ_{d2eGFP}, as the same symmetry effects as for γ_{eGFP} could be expected. However, the estimated degradation rates for mRNA and protein are so close to each other that symmetry has a negligible effect. For the mRNA degradation rate δ, the STS approach yields different distributions depending on the considered dataset, while the NLME, by construction, yields a single consistent distribution. For γ_{eGFP}, the NLME yields a narrower distribution than the STS approach. This narrowing of the distribution can be attributed to the breaking of the parameter symmetry through the consideration of an additional dataset. (see Methods, Section Uncertainty Analysis of Single-Cell Parameters). This demonstrates that only the NLME approach is able

to convey meaning to single-cell perturbation experiments. Indeed, by breaking the symmetry, the NLME approach improves
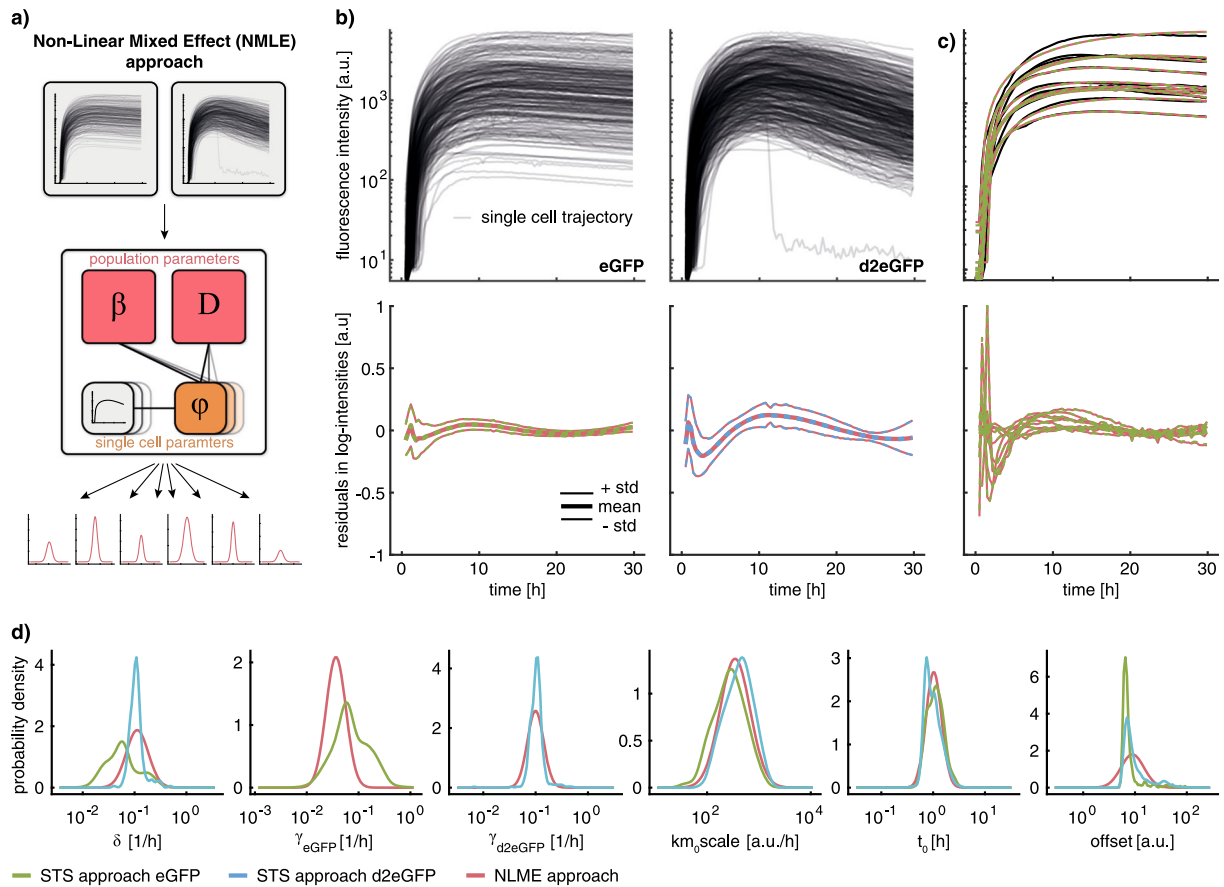
Fig. 3 Comparison of parameter estimation results for the NLME and STS approaches. Coloring indicates employed approach (STS, NLME) and dataset (eGFP, d2EGFP). **a** Schematic illustration of the NLME approach. **b** Experimentally recorded single-cell eGFP and d2eGFP trajectories (top) and population statistics of residuals for the investigated approaches (bottom). **c** Exemplary fits for 10 representative single-cell trajectories (top) and corresponding residuals (bottom). **d** Comparison of parameter distributions computed using the STS and the NLME approach

not only the estimates of population parameters such as mean and variance, but also estimates of single-cell parameters (Fig. S2).

Model selection indicates rate limitation through ribosome abundance

To assess the appropriateness of the fitting results achieved using the STS and NLME approaches for modeling, we computed the distribution of the residuals at different time points. The result revealed a clear temporal trend (Fig. 3b), indicating that the considered mechanistic model was insufficient to describe the data. For this reason, we analyzed three additional models (Fig. 4a (ii)–(iv)) that take the effect of ribosomes in protein translation and enzymes on mRNA degradation into account. The effect of enzymes on protein degradation was not supported by experimental evidence and accordingly not included in any candidate model (see Methods, Section Structure of Models for GFP Translation, Fig. S1). In contrast, the proposed extensions are supported by experimental evidence collected in other studies.[45] Yet, the relevance of these processes for single-cell transfection dynamics has not been studied in detail.

The effect of ribosomes is modeled by introducing the ribosomal species with initial free concentration R_0, which binds to the mRNA at rate k_1 (Fig. 4a (ii)). The translation happens at rate k_2 and produces a free mRNA molecule and a free ribosome. The effect of enzymatic degradation is modeled by introducing an enzymatic species with initial free concentration. The degradation reaction of the mRNA is replaced by a binding reaction to the enzyme with rate δ_1 (Fig. 4a (iii)). The enzyme degrades the bound

mRNA molecule with rate δ_2. In the standard model, these reactions are approximated by first order kinetics, which is reasonable under the assumption that the abundance of ribosomes and enzymes are not rate limiting. In total we considered four different models (Fig. 4a): (i) the standard model with two extensions that feature (ii) ribosomal binding to mRNA before translation, as well as (iii) enzymatic degradation of mRNA and (iv) the combination of both extensions.

We inferred the parameters of models (i)–(iv) using the multi-experiment NLME approach. The corresponding optimization problem was solved using multi-start local, gradient-based search, which provided reproducible estimates (Fig. S4). The comparison of estimated parameters revealed striking differences (Fig. 4b), in particular for the degradation rates δ, γ_{eGFP}, and γ_{d2eGFP}. This highlights the need for appropriate models when estimating these kinetic parameters.

To select among candidate models, we considered the model selection criteria Akaike Information Criterion (AIC)[46] and Bayesian Information Criterion (BIC).[47] AIC and BIC favored the two models with ribosomal translation (Fig. 4c), model (ii) and (iv). The best AIC and BIC values were achieved by model (iv)—the most complex model—accounting for ribosomal translation and enzymatic degradation. Closer inspection revealed that the AIC and BIC values are dominated by the value of the log-likelihood function. The contribution of the complexity penalization is minor, which suggests that decisions based on these AIC and BIC values might be misleading. This was also observed in a recent single cell study considering population snapshot data.[16]
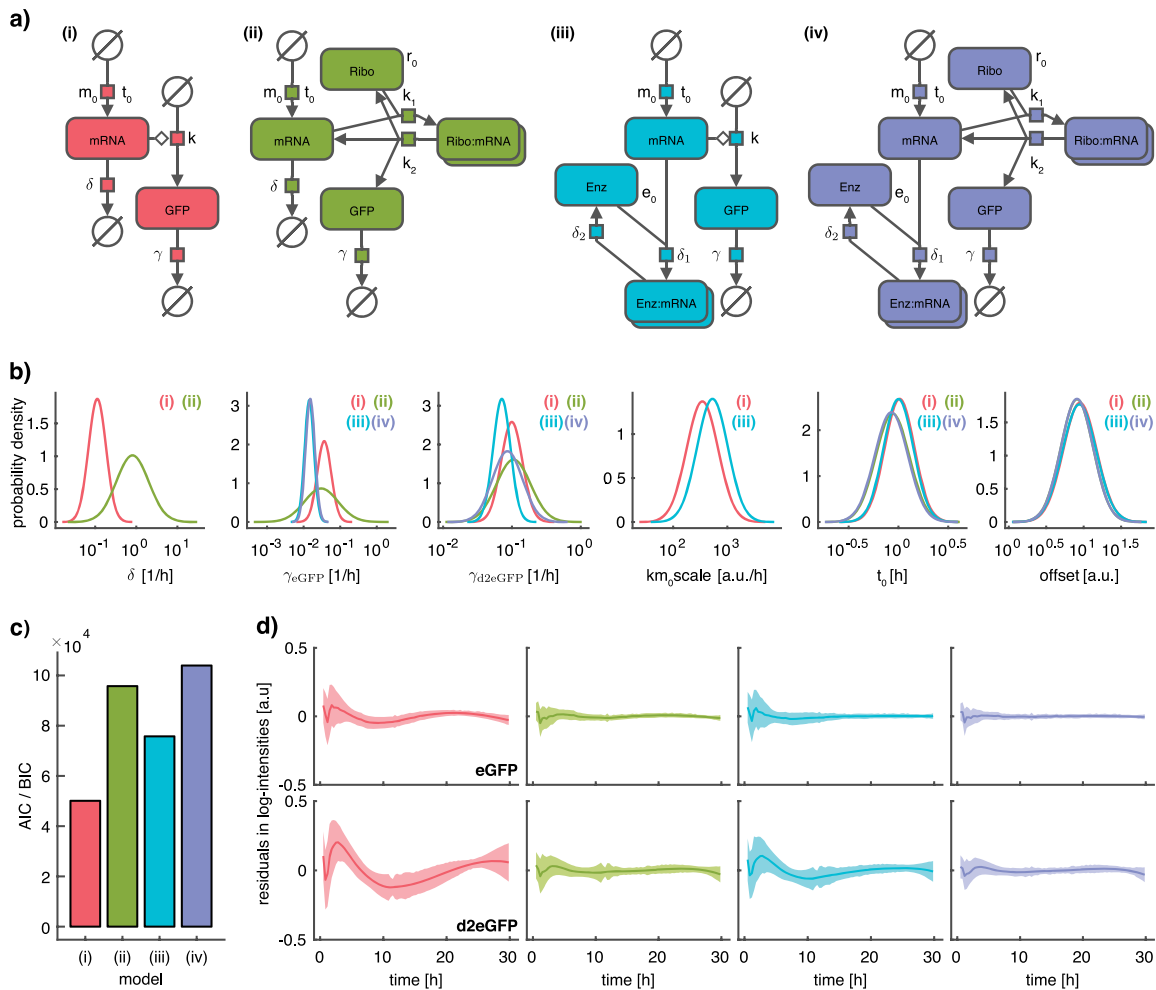
Fig. 4 Comparison of parameter estimation results for four model candidates. Coloring corresponds to the model. **a** Systems Biology Graphical Notation (SBGN) representation of the four model candidates with parameters plotted next to the respective reactions. The SBGN representation was created using the Newt editor.[60] **b** Comparison of parameter distributions across all considered models according to the NLME approach. Distributions are only shown for those models that include the respective parameter, as indicated by models numbers in each subplot. **c** Comparison of AIC/BIC values for MLE estimate for the four different models. AIC and BIC values are visually indistinguishable and thus depicted as single bar. **d** Comparison of residuals for the four model candidates. Top: eGFP, bottom: d2eGFP. Shaded areas correspond to +/− one standard deviation across single-cells

To follow up on these findings, we evaluated the time-dependent residual distribution (Fig. 4d). This revealed that the magnitude of the residuals is substantially smaller for models with ribosomal translation (ii, iv) compared to models which do not account for this mechanism (i,iii). This suggests that the approximation of the ribosomal translation process with first order kinetics is not appropriate and that the abundance of free ribosomes is rate-limiting. In contrast, the difference in the residual profiles for model (ii) and (iv) is small, suggesting that enzymatic degradation is not essential to describe the data. For this reason, we perform all subsequent analyses with model (ii).

Mechanistic model identifies and explains batch effects
The experimental setup used in this study allowed for the investigation of multiple perturbation conditions in a single experimental batch. This is not always possible and each experimental condition often has to be investigated in an individual batch, which makes it difficult to distinguish perturbation specific effects from batch effects. Moreover, studies considering single-cell data sometimes pool batches to increase the statistical power,[33] which makes it difficult to distinguish single-cell heterogeneity from batch effects. Hence, robustness to

batch effects is required for the meaningful integration of multiple (pooled) perturbation experiments.

To assess the robustness and reproducibility of our results, we recorded two additional experimental replicates, i.e., two additional batches. All replicates provide single-cell trajectories for >200 cells per experimental condition over a duration of ~30 h. For each experimental replicate, the single-cell trajectories were split into 3 subsets of same size, resulting in a total of 9 datasets (Fig. 5a). Even for our highly quantitative experimental setup, we found differences between replicates, which are larger than the sampling error (Fig. 5b).

To assess the effect of these batch effects on parameter estimates, we performed parameter estimation using the NLME approach for all 9 subsets individually. For all replicates, we observed similar average log-likelihood values, suggesting that the fit to all three datasets was of a similar quality (Fig. 5c). In contrast, we observed a much higher variability of log-likelihood values across the different subsets compared to individual replicates. As the log-likelihood is equal to the sum over independent contributions of individual single cells, the standard deviation of the log-likelihood can be assumed to scale linearly with the number of considered cells. Consequently, the standard deviation can be extrapolated to the full experiment by dividing
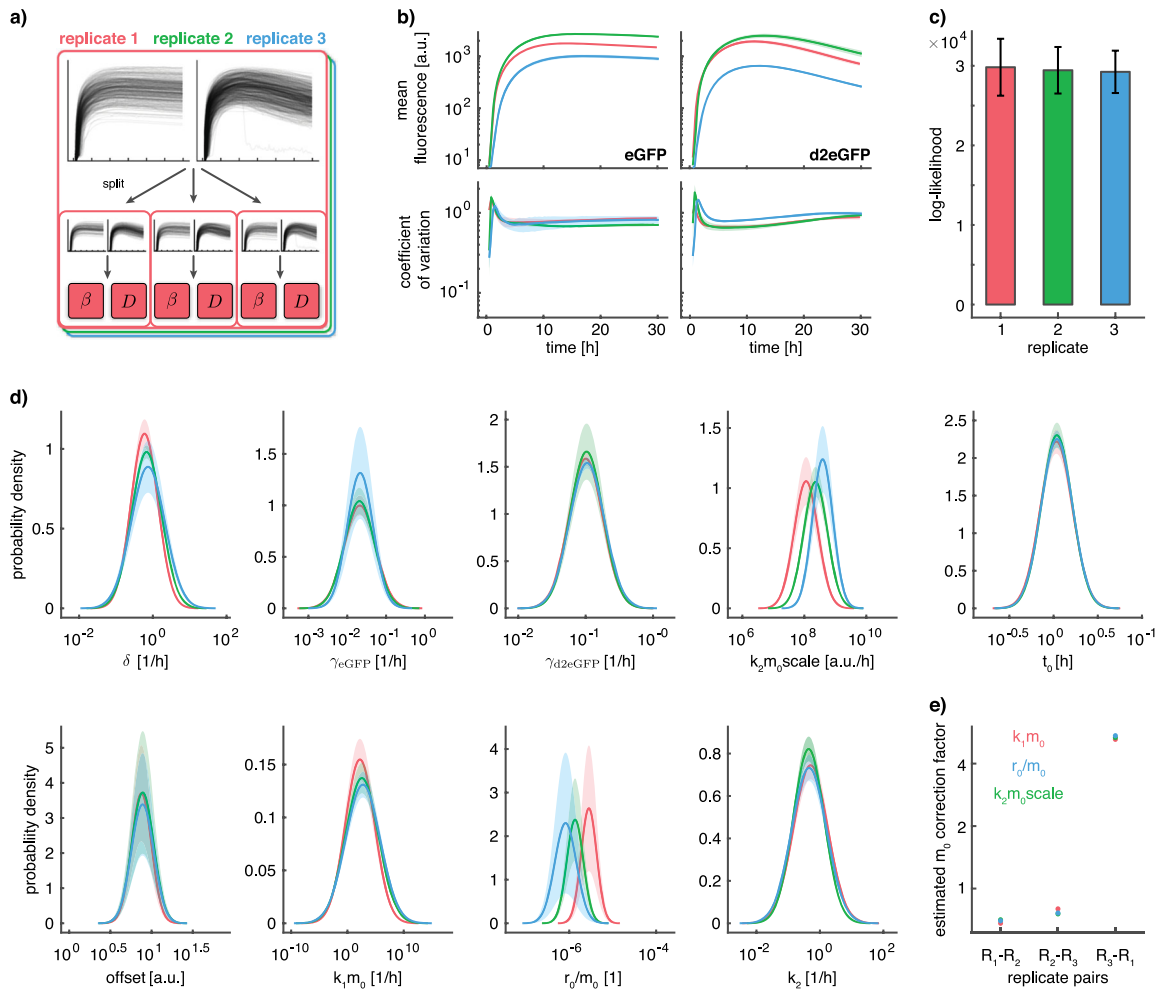
Fig. 5 Uncertainty analysis for parameter distributions for model with ribosomal translation. Coloring according to replicate. **a** Illustration of replicates and threefold split in data subsets. **b** Comparison of variability of mean and coefficient of variation within and across replicates. Shaded areas indicate sampling error and correspond to $+/-$ one standard deviation within replicates. **c** Comparison of log-likelihood within and across replicates. Error bars correspond to $+/-$ one standard deviation within replicates. **d** Analysis of uncertainty of parameter distributions within and across replicates. Shaded areas correspond to $+/-$ one standard deviation within replicates. **e** Estimated correction factors for m_0 according to the respective estimated parameter distributions. Coloring according to the parameter distribution used to compute the correction factor

with the square root of the fraction of considered cells $\left(\sqrt{\frac{1}{3}} \approx 1.732\right)$. This allowed us to compute the standard deviation of the log-likelihood values for the full experiment, which was considered for the analysis in Fig. 4c and accordingly test whether the observed difference in log-likelihood values for individual models is statistically significant. We found that the difference in log-likelihood value between model (i) and (ii) is statistically significant ($p = 0.018$), while the differences between model (ii) and (iii) ($p = 0.084$) and between model (ii) and (iv) ($p = 0.317$) are not statistically significant.

The estimated parameter distributions were largely consistent within, as well as across replicates (Fig. 5d). The only parameters for which we found apparent differences were $k_2 m_0 scale$, $k_1 m_0$ and R_0/m_0 (due to the width of the densities for $k_1 m_0$, the differences in $k_1 m_0$ are hard to spot by eye). For these parameters, the population means differed substantially across replicates. All three parameter combinations contain the parameter m_0, which describes the average concentration of mRNA transfected into the cells. In fact, since transfection efficiency is sensitive to cell culture conditions and the exact timing in the transfection preparation, it is likely that the experiment–to–experiment variability of the parameter m_0 exceeds the intrinsic width of the parameter

distributions of a single experiment. We found that the computed correction factors for m_0 are consistent for all parameters and replicates (Fig. 5e). This suggests that differences in the average number of mRNA molecules released into the cytoplasm can indeed explain the observed batch effects, and shows that the NLME approach allows for the identification and handling of batch effects.

DISCUSSION

Single-cell time-lapse experiments are essential for the quantification and unraveling of the dynamics of cellular processes at the single-cell level. The NLME approach provides a powerful statistical tool to analyze single-cell fluorescence trajectories.[25,26,33,34] In this study we introduced the multi-experiment NLME approach and demonstrated how it can be used to integrate single-cell measurements from multiple perturbation experiments. In particular, we studied eGFP expression after mRNA transfection using two distinct eGFP variants with different protein lifetime. The integration of these two datasets into a multi-experiment non-linear mixed effect modeling allowed for the robust parameter estimation. In particular, the reliable estimation of the distribution of mRNA lifetime, the key parameter of interest,

is now possible for the standard model. Interestingly, the integration of data on the population level also improves the estimates of single-cell parameters by eliminating the structural non-identifiability (Fig. S2). The multi-experiment integration is an important advancement. Generally, experiments are measured using the same readouts under different experimental conditions, which essentially alters the entire set of parameters and does not change the quality of the parameter estimation.

The parameter estimation was performed using a gradient-based approach, which yields consistent results within, as well as across replicate experiments, i.e., individual optimization runs consistently converged to similar likelihood values. Still, as observed in other studies,[48] we found that the convergence frequency of the local optimizers to the global optimum decreases as the model complexity increases (see Methods, Section Reproducibility of Optimization Results for the NLME Approach, Fig. S4). Moreover, although the current implementation of the approach scales linearly with respect to the number of considered single cells, application to higher throughput experiments may be problematic due to the already high computational cost for hundreds of cells.

The single-cell resolution allowed us to identify a pronounced temporal structure in the residuals of the established standard model of gene expression. This assessment revealed a substantial limitation of the established model and can directly be employed in other studies. Our model selection revealed improved agreement with a model that includes ribosomal rate-limitation of translation. Still, the residuals of the proposed model show a temporal structure and a higher magnitude for early time points (Fig. 4d). The experimental data show smoother onset dynamics than the model simulations (Fig. 4d, column 2), which could be explained by including GFP maturation or a more complex transfection process. The time-distributed delivery of multiple individual lipoplexes or a maturation phase of the protein would both be possible explanations for the smoother onset dynamics.

We find that for some of the parameters the population variability is estimated to be surprisingly large (e.g., $k_1 m_0$ in Fig. 5). This may be due to a combination of large variabilities in k_1 and m_0. Alternatively, the description of the transfection or the translation process might still be too simple, and that the variability accumulating along multi-step processes is compensated by a large variability of few parameters.[5] As in similar studies, the results depend on the underlying mechanistic and statistical model. A refinement might improve the estimation accuracy further. Here, we see our results corroborated by the generally good agreement between literature values and the population mean parameter estimated with the NLME approach (Tab. S2).

In this study, well-established prior knowledge motivated the assignment of different degradation rate distributions to individual experimental conditions. In other settings, the assignment of parameter distributions to experimental conditions may not be evident *a priori* and a data driven elucidation of the respective assignment structure may be desirable. This could be achieved by performing model selection on different assignment structure candidates. As the number of different assignment structure candidates may be large, scalable approaches such as L1 penalization[16] are likely to be necessary for such an analysis. For such an analysis, the use of multi-experiment NLME would be indispensable, as the respective assignment structure cannot be represented in an STS approach.

All our findings were reproducible across independent experimental replicates. However, we found that batch effects arise even in sophisticated pipelines. In single-cell studies, these batch effects are often not handled adequately or hidden by pooling cells. Here, we demonstrated that the NLME approach can identify sources of batch effects, a crucial step to improve the experimental processes.

In summary, the NLME approach provides a powerful tool for the analysis of single-cell data with many possible extensions.[25,26,31] We have demonstrated that the usefulness of the NLME approach is not limited to settings with sparse and noisy data, but also extends to settings where multiple experiments are considered. We anticipate that this unique feature of the NLME approach will help unraveling more mechanistic details about basic processes such as gene expression, but also enable careful design of targeted treatment strategies with mRNA-based therapeutic agents. Hence, we advocate the synergistic use of multiple datasets and their integration using the NLME approach to unravel underlying mechanisms and potential sources of batch effects.

METHODS

Materials
RPMI 1640, Leibovitz's L15 Medium, and Trypsin-EDTA were purchased from c.c.pro GmbH, Germany. FBS, HEPES solution, Sodium pyruvate, OptiMEM, and Lipofectamine[TM] 2000 were purchased from Invitrogen, Germany. Sterile PBS was prepared in-house. Six-channel slides (sticky μ-Slide VI[0.4]) and uncoated coverslips were purchased from ibidi, Germany. PLL(20 kDa)-g[3.5]-PEG(2 kDa) was purchased from SuSoS AG, Switzerland. Fibronectin was purchased from Yo Proteins, Sweden. For fluid handling on the microscope the selfmade tubing system was built of PTFE Microtubing with an inner diameter of 0.3 mm (Fisher Scientific, Germany), needlefree swabable valves (MEDNET, Germany), female luer lugs (MEDNET, Germany), and in-house made male luer teflon plugs.

Plasmid vectors and mRNA production
Open reading frame of Enhanced Green Fluorescent Protein (eGFP), as well as from Destabilized Enhanced Green Fluorescent Protein (d2eGFP) was excised from peGFP-N1 and pd2EGFP-N1, respectively (Clontech) and cloned into the backbone pVAX1-A120 which has been described previously[49] to generate pVAXA120-eGFP, as well as pVAXA120-d2EGFP.

The resulting plasmids were further linearized downstream of the poly (A) tail by NotI digestion and purified by chloroform extraction and ethanol precipitation. Purified linear plasmids were used as template for mRNA production via in vitro transcription (IVT) using RiboMax Large Scale RNA production System-T7 (Promega, Germany). Along with the addition of Anti-Reverse Cap Analog (ARCA) into to the IVT reaction mix to generate 5′ capped mRNA, chemically modified nucleotides, namely methyl-CTP and thio-UTP (Jena Bioscience, Germany), were added into reaction for the production of chemically modified mRNAs (cmRNAs) as described by Ferizi et al.[10] The final RNA pellet was resuspended in RNAse free water and stored at −80 °C.

Cell culture
The human hepatoma epithelial cell line HuH7 (I.A.Z. Munich, Germany) was cultured in RPMI 1640 medium, supplemented with 10% FCS, 5 mM HEPES and 5 mM Sodium pyruvate. The cell line was cultured in a humidified atmosphere at 37 °C and 5% CO_2 level.

Surface patterning and array preparation
The single cell arrays are produced using microscale plasma-initiated protein patterning (μPIPP) on a polymer substrate as described in previous work.[10,50] In this study we used uncoated coverslips as substrate for the micropatterning which were glued to adhesive six-channel slides. Each bottom of the six channels is microstructured with the same pattern made of 30 μm × 30 μm adhesion squares, which are coated with Fibronectin, and a distance of 60 μm between the squares. The interspace between the Fibronectin squares is passivated with PLL(20 kDa)-g[3.5]-PEG(2 kDa). A detailed protocol of the array fabrication and the advantage of single-cell arrays is published in Reiser et al.[38]

HuH7 cells were seeded at a density of 10,000 cells per channel. The slide was stored in the incubator for four hours to enable cellular self-organization and adhesion on the Fibronectin squares.[51] Afterwards, two tubing systems each linking three of the six channels are connected with the slide enabling perfusion during the time-lapse measurement. The cell culture medium in the channels is exchanged to L15 medium containing 10% FBS by a syringe which is plugged in each of the swabable valves. The

tubing systems were reused for all experiments after rinsing them with 70% EtOH followed by distilled water and autoclaving them.

Time lapse microscopy

The time-lapse imaging was done on a motorized inverted microscope (Nikon, Eclipse Ti-E) equipped with an objective lens (CFI PlanFluor DL-10×, Phase 1, N.A. 0.30; Nikon). A heating chamber (ibidi GmbH, Germany) was used for controlling the sample temperature to 37 °C (± 2 °C) during the measurement. For image acquisition we used a cooled CCD camera (CLARA-E, Andor), a LED light source (SOLA SE II, lumencor), and a filter cube with the filter set 41 024 (CHROMA Technology Corp., Bp450–490, FT510, LP 510–565).

The six-channel slide connected with the tubing systems is put in the heating chamber and all tubes are fixed on the microscope stage for the time lapse measurement. The scanning macro containing information such as the exposure time, as well as the position list is defined prior to the time-lapse measurement using NIS-Elements Advanced Research software (Nikon). The image acquisition was started right after adding the lipoplex solution to the cells. Fluorescent images were recorded every 10 min over a duration of 30 h.

In vitro transfection on the microscope

The cells were transfected with Lipofectamine™ 2000 complexes containing one of the described mRNA constructs. Both mRNA constructs were treated with Lipofectamine™ 2000 using the following protocol: The lipoplexes are made of a ratio of 2.5 µl Lipofectamine™ 2000 per 1 µg mRNA. mRNA and Lipofectamine™ 2000 were diluted separately in OptiMEM in a final volume of 250 µl each and incubated for 5 min at room temperature. The mRNA solution and the Lipofectamine™ 2000 were mixed and further incubated for 20 min at room temperature for lipoplex formation. The final lipoplex solutions have a total volume of 500 µl with a mRNA concentration of 0.5 ng/µl.

During the lipoplex formation the cells were washed with 37 °C warmed-up PBS. After the incubation each of the tubing systems were rinsed with 500 µl of one of the mRNA lipoplex solutions. The time point when the lipoplex solution was added to the cells is defined as the beginning of the experiment. After 1 h of lipoplex incubation the cells were washed with 37 °C warmed-up L15 medium supplemented with 10% FBS and the cells were not treated further for the remaining measurement.

Data acquisition and quantitative image analysis

The obtained raw image stacks of the time-lapse experiments were processed using in-house written plugins in ImageJ for background correction and readout of the single-cell trajectories.[10] First, the image stacks were background corrected based on a previously published algorithm.[52] Afterwards, the fluorescence trajectories were generated by calculating the mean intensity over time for every cell on the micropattern, which expressed the fluorescent protein. To read out the fluorescence trajectories, a grid corresponding to the micropattern is aligned to every image stack and only squares occupied by a cell are manually selected to calculate the mean intensity of the square for every frame of the image stack.

Analysis of processed data suggested a constant offset and multiplicative measurement noise in the recorded fluorescence trajectories. Therefore, we log-transformed the data, which yields additive noise for which standard algorithms can be used. The log-transformation is also applied to observable map in the models, which will be described in the following section. The model also includes a scaling and offset parameter, which is estimated along with the other model parameters.

Structure of models for GFP translation

Translation is a complex process with multiple, potentially rate limiting steps. In this study, we considered four different models: (i) the standard model with two extensions that feature (ii) ribosomal binding to mRNA before translation, as well as (iii) enzymatic degradation of mRNA and (iv) the combination of both extensions.

We also considered the possibility that GFP degradation is enzymatically catalyzed and rate limiting. However, Corish and Tyler-Smith showed that fluorescent reporter proteins, like eGFP, are normally very stable and resistant to enzymatic degradation and can be described with a first order degradation kinetic.[53] For d2eGFP this is not necessarily the case because of the addition of a C-terminal PEST sequence. The PEST motif is naturally found in short-lived proteins and is known to be important for fast protein turn-over.[54] Li et al. showed that eGFP is stable even in presence of the translation block cycloheximide but that d2eGFP is very unstable due to the PEST sequence.[55] To prove that in our experimental set up the protein degradation of both reporter proteins can be described by first order kinetics we did a translation block experiment for cells expressing d2eGFP. We observe single-cell protein degradation after adding the translation inhibitor cycloheximide 7 h post transfection (Fig. S1). A simple exponential decay provided a good fit to all observed fluorescence intensity tracks, implying the sufficiency of first order kinetics in the considered concentration range.

Mathematical models for GFP translation

In the following, we provide model equations for all four considered models of GFP transfection. For all models, we initially derived a basic form of the model and then identified structurally non-identifiable parameters using the MATLAB toolbox GenSSI.[44] Subsequently, we applied state transformation and conservation laws to eliminate structural non-identifiabilities and unnecessary state equations. The model simulations were all carried out using the AMICI toolbox.[56,57] We provide AMICI and SBML implementations of the model on Zenedo (https://doi.org/10.5281/zenodo.1228898). The ODEs for model (i)–(iv) are provided in Table S1.

The models consider up to four state variables: mRNA abundance (m), protein abundance (p), ribosome abundance (r), enzyme abundance (e), ribosome-mRNA complex abundance (rm), and enzyme-mRNA complex abundance (em). All models include the bolus injection which increases the mRNA level at time t_0 from 0 to m_0,

$$\lim_{t \to t_0, t < t_0} m'(t) = m'(t) + m_0.$$

In the transformed models, we consider the normalized mRNA abundance, $m = m'/m_0$, yielding for the bolus injection

$$\lim_{t \to t_0, t < t_0} m(t) = m(t) + 1$$

The bolus injection is not explicitly described in Table S1. Instead, we write $m(t_0) = m_0$ and $m'(t_0) = 1$. The mRNA abundances are 0 up to time t_0.

Uncertainty analysis of single-cell parameters

To assess the effect of the population constraint on single-cell parameter estimates, we analyzed the respective uncertainty for the STS and the NLME approach using the profile likelihood approach.[58] The analysis revealed that the uncertainty of parameters km_0scale, t_0 and $offset$ is negligible compared to the population variability (Fig. S2a). Moreover, there are only small differences in the location of the mode and the width of the profiles between the two approaches, which suggests that the imposition of the population constraint in the NLME approach has negligible effect on the estimated values for these parameters. For δ and γ_{eGFP} the profiles for the STS approach are bimodal, which can be expected due to the parameter symmetry. For the single-experiment (eGFP dataset) NLME approach, the separation of modes increased compared to the STS approach, but parameter symmetry persisted. For the multi-experiment NLME approach, the profiles become unimodal, which indicates that the symmetry has indeed been broken.

A careful inspection of profiles revealed that a large number of profiles of δ and γ_{eGFP} are unimodal instead of bimodal. This effect can be explained by the superposition of uncertainty of the two modes that would be expected according to parameter symmetry. To demonstrate this effect, we approximated the profile shown in Fig. S2a as sum of two normal densities (Fig. S2b). For the investigated case, a change in the mean of the normal densities, as small as 1% of the parameter value, led to the emergence of a single mode in the middle between the two previous modes. As δ and γ_{eGFP} are symmetric, a unimodal profile implies that both parameters are estimated to the same value. Consequently, the STS approach fails to resolve sufficiently small differences between δ and γ_{eGFP} and instead estimates both parameters to be the same (Fig. S1c). In this study, this leads to a trimodal shape of the parameter population density (Fig. 2d), where two of the modes are explained by the symmetry of parameters for which the difference was sufficiently big, while the third mode is explained by the remaining parameter for which the difference could not be resolved. Overall, this phenomenon introduces a bias in the estimates of the single-cell parameters, as well as the population level distributions.

For the NLME approach, we do not directly observe this effect, as all profiles are unimodal. However, we found that some of the single-cell profiles are slightly skewed. This might be the reason for the slight skewness in the estimated density of single-cell parameters (Fig. S2d). Yet, as the NLME approach assumes a normal density, this skewness is not present in the estimated population variability.

Literature validation of estimated parameter values

Our structural identifiability analysis revealed that only few of the kinetic rates could be uniquely estimated as for most only the products of rates were identifiable. For the uniquely identifiable mRNA degradation rate δ and the protein degradation rates of γ_{eGFP} and γ_{d2eGFP} we were able to compare the estimated values to literature values from bulk experiments (Table S2).

STS approach

For the STS approach, we used a standard Maximum Likelihood method to estimate parameters. We transformed the data and assumed additive, independent, normally distributed measurement noise with variance σ_i^2. This yields the likelihood function

$$p\left(\underline{y}_j^{(i)}|\theta_i\right) = \prod_{j=1}^{n_t} \frac{1}{\sqrt{2\pi\sigma_i^2}} \exp\left(-\frac{\left(\underline{y}_j^{(i)} - y(t_j, \theta_i)\right)^2}{2\sigma_i^2}\right),$$

where $\underline{y}_j^{(i)}$ is the measurement data for cell i and the vector θ_i contains the unknown single-cell model parameters. In a single-cell context, no empirical estimator, which requires multiple replicates, can be used to estimate σ_i^2 from data, as we are limited to a single replicate per single cell. Therefore, we use the model-based estimate of σ_i^2 [29]:

$$\sigma_i^2 = \sum_{j=1}^{n_t} \frac{(\underline{y}_j^{(i)} - y(t_j, \theta))^2}{n_t}$$

To estimate the parameters θ_i, the optimization problem

$$\hat{\theta}_i = \text{argmax}_\theta p(\underline{y}^{(i)}|\theta)$$

is solved for every cell using a local gradient-based multi-start algorithm implemented in the Matlab toolbox PESTO.[59] AMICI[56] was used for the computation of the gradient. The convergence was checked by comparing the best estimates. The population densities were then computed based on a kernel density estimate.

NLME approach

For the NLME approach, we replace the parameter θ_i by a mixed effect φ_i which consists of a fixed effect β and a random effect $b_i \sim N(0, D)$. To compute the likelihood for the NLME model, we have to evaluate an integral over the random effects[29]:

$$p\left(\underline{y}|\beta, D\right) = \prod_{i=1}^{n_c} \int p\left(\underline{y}^{(i)}|\varphi_i = \exp(\beta + b_i)\right) p(b_i|D) db_i,$$

where n_c is the total number of cells. Numerically exact evaluation of this integral with methods such as Markov Chain Monte Carlo sampling is computationally highly demanding. Instead, we used the Laplace approximation.[29] The Laplace approximation assumes that $\psi_i(b|\beta, D) = \log\left(p\left(\underline{y}^{(i)}|\varphi_i = \exp(\beta + b_i)\right) p(b_i|D)\right)$ is close to a quadratic function in b, which allows analytic evaluation of the integral for the approximate likelihood $\underline{p}$:

$$\underline{p}\left(\underline{y}|\beta, D\right) = \prod_{i=1}^{n_c} \exp\left(-\frac{1}{2}\psi_i(\hat{b}_i|\beta, D) + \frac{1}{2}\log\left((2\pi)^{n_b}\right)\det\left(H\psi_i\left(\hat{b}_i|\beta, D\right)\right)\right)$$

$$\text{s.t.} \hat{b}_i = \text{argmin}_b \psi_i(b|\beta, D)$$

where $\left(\hat{\beta}_{NLME}, \hat{D}_{NLME}\right) = \text{argmax}_\theta \underline{p}(\underline{y}|\beta, D)$ is the Hessian of $\psi_i(\hat{b}_i|\beta, D)$. To estimate the population parameters with the NLME approach, we solved a hierarchical optimization problem with the outer problem

$$\left(\hat{\beta}_{NLME}, \hat{D}_{NLME}\right) = \text{argmax}_\theta \underline{p}(\underline{y}|\beta, D)$$

and the inner problem

$$\hat{b}_i = \text{argmin}_b \psi_i(b|\beta, D)$$

The computation of $\underline{p}(y|\beta, D)$ including the respective inner optimization problem was solved using the MATLAB toolbox MEMOIR (https://github.com/ICB-DCM/MEMOIR). In contrast to other NLME modeling toolboxes such as MONOLIX or NONMEM, MEMOIR employs local-gradient based optimization algorithm, which uses AMICI[56] for the computation of the gradient. The outer optimization problem was solved using Matlab toolbox PESTO,[59] using the interior-point algorithm implemented in FMINCON, initialized and 200 random starting points. MEMOIR was evaluated using a range of artificial data, which are included as examples in the repository.

For the covariance matrix, we used a Matrix Logarithm parameterization.[29] The Matrix Logarithm parameterization guarantees that D is symmetric and positive definite and only uses a minimal number of parameters to prevent overparameterization. For the purpose of this study, we assumed that D has diagonal form, which is equivalent to the assumption that random parameters are independent. Pairwise dependencies can be implemented by a full parameterization of D.

Multi-experiment extension of the NLME approach

The NLME approach per se, is not directly applicable to multiple experiments. We extended the approach by introducing experiment specific single-cell parameters $\varphi_i^e(\beta^e, b_i^e)$. The corresponding likelihood function has to be computed separately per experiment

$$p(\underline{y}|\beta, D) = \prod_{e=1}^{n_e} \prod_{i \in E(e)} \int p\left(\underline{y}^{(i)}|\varphi_i^e = \exp(\beta^e + b_i^e)\right) p^e(b_i^e|D^e) db_i^e,$$

where n_e is the number of experiments, $E(e)$ denotes the set of indices of cells belonging to a particular experiment and p^e is the density of the experiment specific population constraint corresponding to $b_i^e \sim N(0, D^e)$. Without loss of generality, it is reasonable to assume that a single cell cannot belong to more than one experiment. The same approximation as before can be applied.

To encode the assumption of conserved quantities, we assume that parameterization of some of the parameters in β^e and D^e are shared across the experiment. For this particular study, we assumed that the parameterization for all parameters, but γ_{eGFP} and γ_{d2eGFP}, is shared across both experiments. For example for model (i), this means that the entries in β^{eGFP} correspond to the parameters [δ, γ_{eGFP}, km_0scale, t_0, $offset$] and in β^{d2eGFP} correspond to the parameters [δ, γ_{d2eGFP}, km_0scale, t_0, $offset$].

Reproducibility of optimization results for the NLME approach

For the NLME approach, we started 200 optimization runs per model (Fig. S4). Each individual optimization run required 1–8 weeks of computation time (>15 years of cpu time in total). Our analysis revealed that the optimization results for model (i) were highly reproducible, as the log-likelihood values for the top 10 optimization runs had low variance. Moreover, only a small fraction of optimization runs crashed, i.e., had repeated failures in the evaluation of the log-likelihood function due to numerical integration problems. For models (ii)–(iv), the variance in log-likelihood value, as well as the number of crashed optimization runs is substantially higher compared to model (i). However, we found that the differences among the top 10 optimization runs for each model were substantially smaller (10^1 to $5 \cdot 10^2$) than differences in log-likelihood values across models (>5–10^3) (Fig. S4). Hence, we do not expect any negative impact on the validity of model selection. To analyze the robustness of parameter estimates, we analyzed the median absolute deviation of parameter values and compared this to the median (Fig. S5). We found that for models (i) and (iii), the median absolute deviation is always substantially smaller than the median value. For model (ii) we could identify a single parameter (variance of R_0/m_0), for which the median absolute deviation is bigger than the median, but median absolute deviation itself is small (<0.01). In Fig. 5d, there was mild uncertainty of the reconstructed distributions of R_0/m_0. The findings here suggest that issues in optimization may have contributed to this uncertainty. For model (iv) these optimization issues may be more severe as more the median absolute deviation is bigger than the median value for more parameters, but still the maximum of these median absolute deviations is also small (<0.1).

REFERENCES
1. Altschuler, S. J. & Wu, L. F. Cellular Heterogeneity: Do Differences Make a Difference? *Cell* **141**, 559–563 (2010).
2. Elowitz, M. B., Levine, A. J., Siggia, E. D. & Swain, P. S. Stochastic gene expression in a single cell. *Science* **297**, 1183–1186 (2002).
3. Buettner, F. et al. Computational analysis of cell-to-cell heterogeneity in single-cell RNA-sequencing data reveals hidden subpopulations of cells. *Nat. Biotechnol.* **33**, 155 (2015).
4. Spencer, S. L., Gaudet, S., Albeck, J. G., Burke, J. M. & Sorger, P. K. Non-genetic origins of cell-to-cell variability in TRAIL-induced apoptosis. *Nature* **459**, 428 (2009).
5. Snijder, B. & Pelkmans, L. Origins of regulated cell-to-cell variability. *Nat. Rev. Mol. Cell Biol.* **12**, 119 (2011).
6. Bodenmiller, B. et al. Multiplexed mass cytometry profiling of cellular states perturbed by small-molecule regulators. *Nat. Biotechnol.* **30**, 858, https://doi.org/10.1038/nbt.2317 (2012).
7. Angerer, P. et al. Single cells make big data: new challenges and opportunities in transcriptomics. *Curr. Opin. Syst. Biol.* **4**, 85–91 (2017).
8. Muzzey, D. & van Oudenaarden, A. Quantitative time-lapse fluorescence microscopy in single cells. *Annu. Rev. Cell Dev.* **25**, 301–327 (2009).
9. Locke, J. C. & Elowitz, M. B. Using movies to analyse gene circuit dynamics in single cells. *Nat. Rev. Microbiol.* **7**, 383 (2009).
10. Ferizi, M. et al. Stability analysis of chemically modified mRNA using micropattern-based single-cell arrays. *Lab a Chip* **15**, 3561–3571 (2015).
11. Uhlendorf, J. et al. Long-term model predictive control of gene expression at the population and single-cell levels. *Proc. Natl. Acad. Sci.* **109**, 14271–14276 (2012).
12. Navin, N. et al. Tumour evolution inferred by single-cell sequencing. *Nature* **472**, 90 (2011).
13. Haghverdi, L., Buettner, M., Wolf, F. A., Buettner, F. & Theis, F. J. Diffusion pseudotime robustly reconstructs lineage branching. *Nat. Methods* **13**, 845 (2016).
14. Spencer, S. L. & Sorger, P. K. Measuring and modeling apoptosis in single cells. *Cell* **144**, 926–939 (2011).
15. Hasenauer, J., Hasenauer, C., Hucho, T. & Theis, F. J. ODE constrained mixture modelling: a method for unraveling subpopulation structures and dynamics. *PLoS Comput. Biol.* **10**, e1003686 (2014).
16. Loos, C., Moeller, K., Fröhlich, F., Hucho, T. & Hasenauer, J. A Hierarchical, Data-Driven Approach to Modeling Single-Cell Populations Predicts Latent Causes of Cell-To-Cell Variability. *Cell Syst.* **6**, 593–603 (2018). e513.
17. Chen, T., He, H. L. & Church, G. M. Pacific Symposium in Pacific Symposium on Biocomputing. *Biocomputing'99* 29–40 (World Scientific, Singapore 1999).
18. Kühn, C. et al. Monte carlo analysis of an ode model of the sea urchin endomesoderm network. *BMC Syst. Biol.* **3**, 83 (2009).
19. Klipp, E., Herwig, R., Kowald, A., Wierling, C. & Lehrach, H. *Systems Biology in Practice: Concepts, Implementation and Application*. (John Wiley & Sons, Weinheim 2008).
20. Kitano, H. Systems biology: a brief overview. *Science* **295**, 1662–1664 (2002).
21. Leonhardt, C. et al. Single-cell mRNA transfection studies: delivery, kinetics and statistics by numbers. *Nanomedicine* **10**, 679–688 (2014).
22. Yamamoto, A., Kormann, M., Rosenecker, J. & Rudolph, C. Current prospects for mRNA gene delivery. *Eur. J. Pharm. Biopharm.* **71**, 484–489 (2009).
23. Kreiter, S., Diken, M., Selmi, A., Türeci, Ö. & Sahin, U. Tumor vaccination using messenger RNA: prospects of a future therapy. *Curr. Opin. Immunol.* **23**, 399–406 (2011).
24. Sahin, U., Karikó, K. & Türeci, Ö. mRNA-based therapeutics—developing a new class of drugs. *Nat. Rev. Drug Discov.* **13**, 759 (2014).
25. Almquist, J. et al. A Nonlinear Mixed Effects Approach for Modeling the Cell-To-Cell Variability of Mig1 Dynamics in Yeast. *PLoS One* **10**, e0124050 (2015).
26. Karlsson, M. et al. Nonlinear mixed-effects modelling for single cell estimation: when, why, and how to use it. *BMC Syst. Biol.* **9**, 52 (2015).
27. Kalita, M. K. et al. Sources of cell-to-cell variability in canonical NF-κB signaling pathway inferred from single cell dynamic images. *J. Biol. Chem.* **M111**, 280925 (2011).
28. Sheiner, L. B. & Beal, S. L. Evaluation of methods for estimating population pharmacokinetic parameters. III. *Monoexponential Model.* **11**, 303–319 (1983).
29. Pinheiro, J. C. *Topics in Mixed Effects Models* PhD thesis, University of Wisconsin - Madison, (1994).
30. Wang, Y. Derivation of various NONMEM estimation methods. *J. Pharmacokinet. Pharmacodyn.* **34**, 575–593 (2007).
31. Kuhn, E. & Lavielle, M. Maximum likelihood estimation in nonlinear mixed effects models. *Comput. Stat. & Data Anal.* **49**, 1020–1038 (2005).
32. Beal, S. & Sheiner, L. The NONMEM System. *Am. Stat.* **34**, 118–119 (1980).
33. Zechner, C., Unger, M., Pelet, S., Peter, M. & Koeppl, H. Scalable inference of heterogeneous reaction kinetics from pooled single-cell recordings. *Nat. Methods* **11**, 197 (2014).
34. Llamosi, A. et al. What population reveals about individual cell identity: single-cell parameter estimation of models of gene expression in yeast. *PLoS Comput. Biol.* **12**, e1004706 (2016).
35. Chis, O.-T., Banga, J. R. & Balsa-Canto, E. Structural identifiability of systems biology models: a critical comparison of methods. *PloS One* **6**, e27755 (2011).
36. Lavielle, M. & Aarons, L. What do we mean by identifiability in mixed effects models? *J. Pharmacokinet. Pharmacodyn.* **43**, 111–122 (2016).
37. Flassig, R. J. & Sundmacher, K. Optimal design of stimulus experiments for robust discrimination of biochemical reaction networks. *Bioinformatics* **28**, 3089–3096 (2012).
38. Reiser, A., Zorn, M. L., Murschhauser, A. & Rädler, J. O. in *Cell-Based Microarrays: Methods and Protocols* (eds Peter Ertl & Mario Rothbauer) 41–54 (Springer New York 2018).
39. Ligon, T. S., Leonhardt, C. & Rädler, J. O. Multi-level kinetic model of mRNA delivery via transfection of lipoplexes. *PLoS One* **9**, e107148 (2014).
40. Liu, Y., Beyer, A. & Aebersold, R. On the dependency of cellular protein levels on mRNA abundance. *Cell* **165**, 535–550 (2016).
41. Darmanis, S. et al. Simultaneous multiplexed measurement of RNA and proteins in single cells. *Cell Rep.* **14**, 380–389 (2016).
42. Frei, A. P. et al. Highly multiplexed simultaneous detection of RNAs and proteins in single cells. *Nat. Methods* **13**, 269 (2016).
43. Raue, A., Kreutz, C., Theis, F. J. & Timmer, J. Joining forces of Bayesian and frequentist methodology: a study for inference in the presence of non-identifiability. *Philos. Trans. R. Soc. A* **371**, 20110544 (2013).
44. Ligon, T. S. et al. GenSSI 2.0: multi-experiment structural identifiability analysis of SBML models. *Bioinformatics* **34**, 1421–1423 (2017).
45. Parker, R. & Song, H. The enzymes and control of eukaryotic mRNA turnover. *Nat. Struct. Mol. Biol.* **11**, 121 (2004).
46. Akaike, H. in *Selected Papers of Hirotugu Akaike* (eds Emanuel Parzen, Kunio Tanabe & Genshiro Kitagawa) 199-213 (Springer, New York, 1998).
47. Schwarz, G. Estimating the dimension of a model. *Ann. Stat.* **6**, 461–464 (1978).
48. Kreutz, C. New concepts for evaluating the performance of computational methods. *IFAC-Pap.* **49**, 63–70 (2016).
49. Kormann, M. S. et al. Expression of therapeutic proteins after delivery of chemically modified mRNA in mice. *Nat. Biotechnol.* **29**, 154 (2011).
50. Segerer, F. J. et al. Versatile method to generate multiple types of micropatterns. *Biointerphases* **11**, 011005 (2016).
51. Röttgermann, P. J., Alberola, A. P. & Rädler, J. O. Cellular self-organization on micro-structured surfaces. *Soft Matter* **10**, 2397–2404 (2014).
52. Schwarzfischer, M. et al. Efficient fluorescence image normalization for time lapse movies. *Proc. Microsc. Image Analysis Appl. Biolo.* **5**, 1–6 (2011).
53. Corish, P. & Tyler-Smith, C. Attenuation of green fluorescent protein half-life in mammalian cells. *Protein Eng.* **12**, 1035–1040 (1999).

54. Wahlers, A. et al. Influence of multiplicity of infection and protein stability on retroviral vector-mediated gene expression in hematopoietic cells. *Gene Ther.* **8**, 477 (2001).

55. Li, X. et al. Generation of destabilized green fluorescent protein as a transcription reporter. *J. Biol. Chem.* **273**, 34970–34975 (1998).

56. Fröhlich, F., Kaltenbacher, B., Theis, F. J. & Hasenauer, J. Scalable parameter estimation for genome-scale biochemical reaction networks. *PLoS Comput. Biol.* **13**, e1005331 (2017).

57. Fröhlich, F., Theis, F. J., Rädler, J. O. & Hasenauer, J. Parameter estimation for dynamical systems with discrete events and logical operations. *Bioinformatics* **33**, 1049–1056 (2016).

58. Raue, A. et al. Lessons learned from quantitative dynamical modeling in systems biology. *PloS One* **8**, e74335 (2013).

59. Stapor, P. et al. PESTO: Parameter EStimation TOolbox. *Bioinformatics* **34**, 705–707 (2017).

60. Sari, M. et al. SBGNViz: a tool for visualization and complexity management of SBGN process description maps. *PloS One* **10**, e0128985 (2015).